Porosity Reduction in New Thin Films of Ceramic Coatings on Stainless Steel by Annealing at Reduced Pressure

G.I. CUBILLOS, M. BETHENCOURT, J.E. ALFONSO, E. RODRÍGUEZ-CASTELLÓN, and E. ROMERO

New ZrO_xN_y thin films were deposited *via* reactive RF magnetron sputtering on stainless steel substrate from a Y_2O_3-doped ZrO_2 (3YSZ) target. In order to reduce their porosity and increase corrosion resistance, the films were annealed at 265 °C in an inert atmosphere at reduced pressure, increasing their density and corrosion resistance in saline solution. The crystal structure of the films was characterized by means of X-ray diffraction, the morphology *via* scanning electron microscopy and atomic force microscopy, and the chemical composition *via* X-ray photoelectron spectroscopy. The corrosion resistance was evaluated using electrochemical techniques based on linear polarization. The results show that the annealing treatment decreases the morphological imperfections of the coatings such as pores and cracks, which allows increasing the corrosion resistance of the substrate-coating system.

https://doi.org/10.1007/s11661-018-4888-5

I. INTRODUCTION

POROSITY of ceramics coatings is a beneficial property in some applications as catalysis where, according to the method of synthesis, it can vary from micro-porosity to macro-porosity, determining the specific catalyst for a chemical reaction. However, when the aim is to employ these coatings as a protective method against corrosion of metal substrates, forming a physical barrier between the electrolyte and the metal to be protected, the presence of porosity is detrimental, because it will accelerate the rate of interaction of the electrolyte with the substrate.[1,2] The corrosion behavior of physical vapor deposition (PVD) ceramic coated in aqueous solutions is an unresolved problem in many cases.[3,4] A surface pore constitutes a channel in the bulk material that conducts the electrolyte to the substrate and facilitates active substrate-electrolyte interaction. The presence of pores quickly deteriorates the coatings, providing direct paths for corrosive electrolytes to reach the coating/substrate interface, where localized galvanic corrosion can be initiated due to the corrosion potential difference between the coating and the metal.[5–7]

The intermediate point in the application of porous coatings constitutes the field of implants, which on the one hand aims at a porous surface that favors cell growth[3] and on the other an implanted part with a high resistance to corrosion in biological fluids.[4,5,8] Achieving a waterproofing of the surface of a ceramic material deposited on a metal, taking advantage of the chemical inertia of the ceramic to increase the resistance to corrosion of the metal, would be very advantageous.

If we try to increase the corrosion resistance of a stainless steel by sintering the ceramic deposited on it, we encounter another disadvantage: the sintering processes are carried out at high temperature, and stainless steels, depending on their chemical composition, can be sensitized by precipitation of the chromium carbides at the grain boundaries.[6] This triggers a loss of its corrosion resistance properties by decreasing the concentration of chromium in the matrix of the steel. The objective of the present research paper is to develop a method that reduces the porosity and the presence of imperfections on the surface of the ceramic at low temperature without altering the properties of the steel. Films with a presence of pores in the ceramic material

---

G.I. CUBILLOS and E. ROMERO are with the Group of Materials and Chemical Processes, Department of Chemistry, Universidad Nacional de Colombia, Av.Cra. 30 No. 45-03, Bogotá, Colombia. Contact e-mail: gcubillos@unal.edu.co M. BETHENCOURT is with the Department of Materials Science, Metallurgy Engineering and Inorganic Chemistry, International Campus of Excellence of the Sea (CEI-MAR), University of Cadiz, Avda. República Saharaui, 11510 Puerto Real, Spain. J.E. ALFONSO is with the Group of Material and Surface Science, Department of Physics, Universidad Nacional de Colombia, Bogotá AA-14490, Colombia. E. RODRÍGUEZ-CASTELLÓN is with the Department of Inorganic Chemistry, Crystallography and Mineralogy (Unit Associated to ICP-CSIC), Faculty of Sciences, University of Malaga, Campus de Teatinos, 29071 Málaga, Spain.

Manuscript submitted February 22, 2018.

undergo an annealing treatment at 265 °C in an inert atmosphere under reduced pressure (ARP), where the increase in grain size seals the imperfections on the surface of the ceramic, favoring its waterproofing without altering its chemical composition.

II. EXPERIMENTAL METHOD

A. *Coating Deposition*

AISI-316L steel substrates of 1.5 × 1.5 cm^2 were polished with SiC at 600 grits and washed with anionic surfactant and abundant water. Organic impurities were removed in an ultrasonic bath for two minutes using acetone and isopropanol. The equipment used to grow the films was an Alcatel HS2000. Films were obtained from a 4″ × ¼″ (Y_2O_3) 0.8 ZrO_2 (92 mol pct) target (99.9 pct), the same target on which a nickel or zinc (99.99 pct) disk was placed. The parameters used were as follows: base pressure 3.4×10^{-1} Pa, total working pressure 8.6×10^{-1} Pa, deposition time 45 min, target-substrate distance 5 cm, Ar (99.999 pct) and N_2 (99.999 pct), and power supplied to the target 250 W, with a N_2 flux of 15.0 sccm and an Ar flux of 20.0 sccm.

ZrO_2Y, ZrO_2YNi, ZrO_2YN15, $ZrO_2YNiN15$, and $ZrO_2YZnN15$ thin films were deposited using a partially stabilized zirconia target with yttria, Ni-ZrO_2, and Zn-ZrO_2. In all cases, the radio frequency (RF) sputtering technique was used. The first four films were deposited at 90 °C and subsequently were subjected to a ARP carried out for two hours in an Ar atmosphere at 265 °C and a pressure of $7.4E^{-1}$ Pa. The $ZrO_2YZnN15$ film was only deposited at 265 °C and then annealed at the same temperature, since when it is deposited at 90 °C, delamination of the coating occurs. Table I summarizes the deposit conditions for each film.

B. *Surface Morphology*

Surface morphology was characterized by scanning electron microscopy (SEM) in a Quanta-2000 working at 15 kV and 10 mA. The thickness of the films was measured with a Veeco-Dektak 150 surface profilometer. Their roughness was determined with a non-contact atomic force microscopy (AFM) Autoprobe-cp Park-Scientific instrument with a tip radius of 10 nm, study area of 4 μm^2, and frequency of 2 Hz.

C. *Chemical Composition*

The surface chemical composition was determined by means of X-ray photoelectron spectroscopy (XPS) using a Leybold-Heraeus LHS-10 spectrometer under a vacuum greater than 3×10^{-8} Pa, with Al Kα radiation (1486.6 eV), and a constant pass energy of 200 eV for the wide-scan spectra and 20 eV for the narrow-scan XPS spectra. At 20 eV pass energy, a full width at half maximum (FWHM) of 0.95 eV for the Ag $3d_{5/2}$ core level was measured. The specimen was sputtered with 2 keV Ar^+ ions for 1 minute in order to eliminate most of the surface contaminants. During the sputter cleaning, the Ar pressure in the analysis chamber was maintained at 3.5×10^{-5} mbar. Under these sputtering conditions, only the uppermost contamination layer (< 1 nm) is removed. Binding energies (BE) referred to the C 1*s* line (284.8 eV) of the adventitious contamination layer.[7] The values of BE are accurate to ± 0.2 eV.

D. *Corrosion Tests*

The corrosion resistance of the films and the stainless steel was evaluated using linear polarization (LP) and polarization resistance (Rp) in a 3.5 pct p/v NaCl solution, using a SI1287-potentiostat (Solartron). A standard three-electrode cell was employed, with a Ag/AgCl reference electrode (0.197 mV/SHE), a working electrode (the coated stainless-steel test piece with an exposed area of 1.00 cm^2) and a counter electrode (graphite). The chemical activities of the samples were analyzed based on the value of Rp calculated through the Stern-Geary equation.[9] The degree of protection was evaluated by comparing this Rp with that corresponding to a bare sample. The polarization in the anodic region was evaluated in order to determine the corrosion resistance of the films.

E. *Crystal Structure*

The crystallographic phases of the coatings were studied *via* X-ray diffraction, using PAN analytical X'PERT equipment with filtered Cu Kα radiation (0.1542 nm) at 45 kV and 40 mA with a step size of 0.02 deg. The corresponding phases were identified by Joint Committee on Powder Diffraction Standards cards (JCPDS). The average crystal size was determined by the Scherrer equation.[10]

$$\beta = \frac{k\lambda}{\mathrm{FWHM}(S)\cos\theta},$$

where β is the crystal size; k is the factor of the crystal and its value is 1.0; λ is the wavelength of the radiation used (λ_{Cu}); θ is the position of the diffraction peak, and FWHM (S) is the width at the mean height of the diffraction peak of the sample.

III. RESULTS AND DISCUSSION

A. *Structure*

Partially stabilized zirconia films with yttria deposited at 265 °C exhibited a cubic structure with preferential growth on the plane (111), while the one deposited at 90 °C grew in a polycrystalline structure with or without ARP (Figure 1(a)). For the zirconium-nickel oxynitride, the behavior of the X-ray profile is similar to that shown for cubic zirconia, where in contrast to this, the crystals have a FWHM the plane (111) greater. This fact can be seen in the enlargement of the signal shown in the upper right of Figures 1(a) and (b).

In the (200) and (400) planes, for zirconia and oxynitride, respectively, no appreciable changes are found, and the resolution of the equipment does not allow differentiation of the sample signal from the noise

Table I. Coating Deposit Conditions

Sample	Composition Coatings T 90 °C	Deposition Temperature (°C)	Thickness (nm)	Flow N_2 (sscm)	Annealing Temperature (°C)
ZrO_2Y	ZrO_2; Y_2O_3	265	500 ± 10	0.00	265
		90	499 ± 15		
ZrO_2YNi	$NiO_{1.13}$; ZrO_2; Y_2O_3	265	494 ± 20	0.00	
		90	450 ± 10		
ZrO_2YN15	$ZrN_{0.40}O_{0.80}$; ZrO_2; Y_2O_3	265	350 ± 11	15.0	
		90	380 ± 16		
$ZrO_2YNiN15$	$NiN_{0.14}O_{0.82}$; $ZrN_{0.15}O_{1.60}$	265	480 ± 20	15.0	
		90	455 ± 10		
$ZrO_2YZnN15$	ZnO; $ZrN_{0.13}O_{1.7}0$	265	375 ± 4	15.0	

Target $Y_2O_30.8ZrO_2$ 92 pct mol.

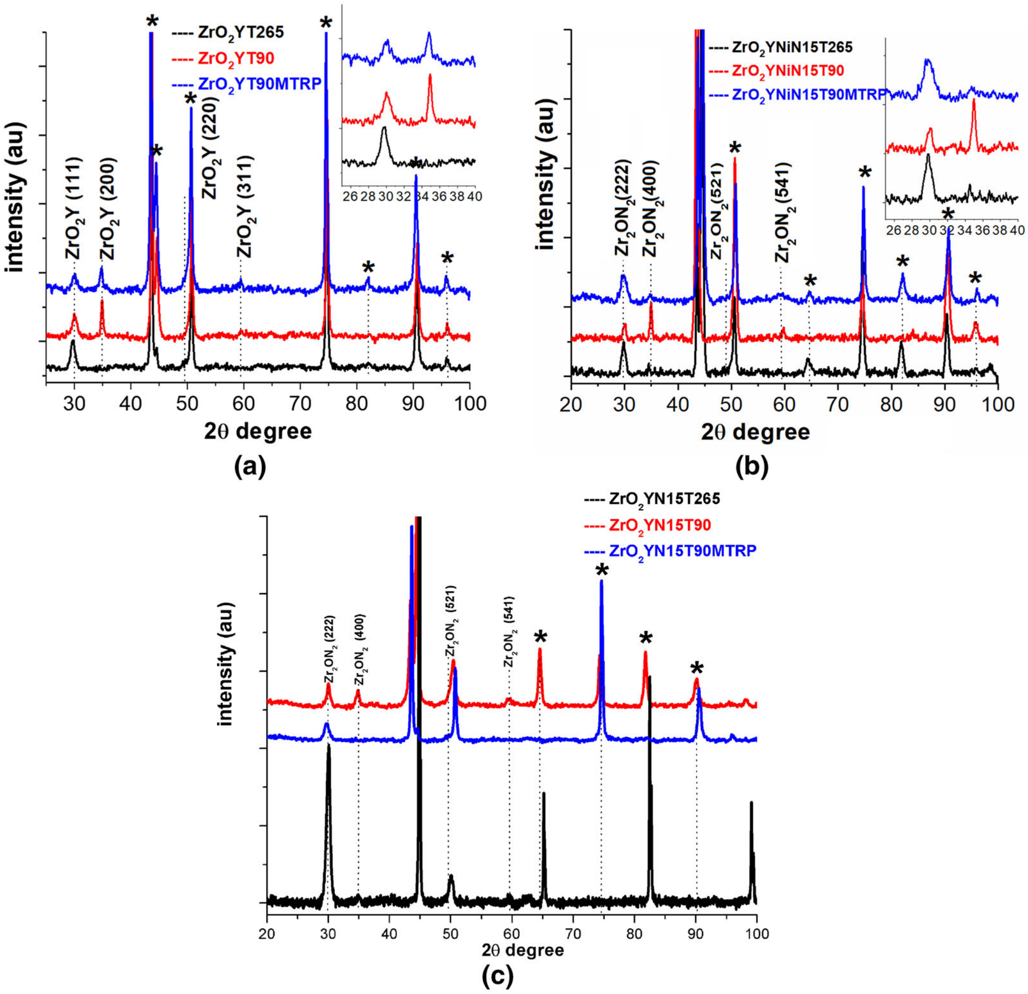

Fig. 1—XRD patterns for coatings deposited at 265 °C, 90 °C and 90 °C ARP: (*a*) ZrO_2Y, (*b*) $ZrO_2YNiN15$, (*c*) ZrO_2N15.

signal for the remaining planes (Figures 1(a) and (c)). The diffraction patterns have been indexed based on JCPDS 00-049-1642 for ZrO_2Y-(*c*) and JCPDS 00-048-1635 for ZrO_2YN-(*c*). Nickel did not influence the crystal structure of the films deposited at 90 °C and 265 °C; however, it inhibited the growth of the plane (400) during the ARP. For the same nickel-free coating, the most crystalline film was deposited at 265 °C.

In general, with a widening towards the full width at half maximum (FWHM), the peak can be seen in films subjected to the ARP. The crystal size determined from the Scherrer equation[10] shows that for films deposited at 265 °C and those annealed at the same temperature in an inert atmosphere, the crystal size is similar and less than 35 pct of the films deposited at 90 °C without ARP for ZrO_2YN15 and 37 pct for $ZrO_2YNiN15$ (Table II).

Table II. Crystal Size for Ceramic Coatings

Sample	Crystal Size (nm)
$ZrO_2YNiN15T90$	23.9
$ZrO_2YNiN15T90ARP$	14.8
$ZrO_2YNiN15T265$	15.4
$ZrO_2YN15T90$	25.4
$ZrO_2YN15T90ARP$	16.0
$ZrO_2YN15T265$	16.9
ZrO_2YT90	18.6
$ZrO_2YT90ARP$	16.2
ZrO_2YT265	17.4

Based on these results, we can suggest that the mechanism by which the ARP favors the decrease in porosity is due to the formation of smaller crystals that are compacted to form larger grains. That is, the density of the grains of the film increases, so that there are a greater number of crystals per grain formed.

The difference between the film deposited directly at 265 °C and the one deposited at 90 °C and later annealed at 265 °C resides in the fact that while in the first the grain is formed directly during the 45-minute deposit, with the ARP treatment, initially smaller grains formed, which during the heat treatment grow in a process four times slower. This process of slow growth of the grains clogs the pores of the coating initially deposited at 90 °C, favoring waterproofing against the corrosive action of the electrolyte during the corrosion process.

B. *Morphology and Corrosion Resistance*

In the present investigation, in order to improve the corrosion resistance of AISI-316L stainless steel, five coatings were deposited. As an example, the results for the samples of ZrO_2Y, ZrO_2YNi, and ZrO_2YZn are shown in Figures 2 through 4, respectively. In the different samples, the microscopy of film A = the film deposited at 265 °C, B = the film deposited at 90 °C, and C = the film deposited at 90 °C ARP. For each one, two magnifications are shown: (a) 1000 or 2000 times to show a panoramic of the surface of the film, and (b) 20,000 times to appreciate the filling of the imperfections after ARP. All the thin films were characterized by being homogeneous; however, the presence of micropores and imperfections on the surface is evident at the two deposition temperatures.

The partially stabilized zirconia film with yttria deposited at 265 °C exhibits micropores (see white arrows, Figure 2(A-a)). If the depositing temperature is 90 °C, in addition to the micropores, there are microcracks (see black arrows, Figure 2(B-a)) possibly associated with low substrate-coating adhesion. However, for the film deposited at 90 °C, after it has been subjected to an ARP carried out for two hours in an Ar atmosphere at 265 °C and a pressure of 7.4E−1 Pa, it can be seen that the treatment is favorable for that surface, since the imperfections are closed, Figure 2(C-b), improving the surface morphology of the ceramic material, possibly by diffusion in the solid state.

To confirm the effectiveness of the heat treatment, 14 pct nickel was added to the ZrO_2Y target in order to increase the presence of micropores. It is well known that ZrO_2-Ni films are highly porous and are therefore used in fuel cells.[11–13] If nickel is added to the film, the presence of imperfections increases, with micropores and microcracks being observed at both temperatures, Figures 3(A) and (B). However, as for the sample without nickel, the coating is also characterized by being homogeneous and by diminishing the presence of superficial imperfections after ARP, Figure 3(C).

For zirconium oxynitride with zinc, a behavior similar to that reported for oxynitrides with and without nickel is observed. SEM shows the presence of abundant micropores, microcracks, and delamination of the film before ARP and an improvement of the surface post ARP (see Figure 4).

Post-treatment surface improvement is evidenced by open circuit (OC) and the potentiodynamic polarization tests as shown in Figures 5(a) and (c) for the four coated samples without nickel and as shown in Figures 5(b) and (d) for samples with nickel. Steel is introduced as an object of comparison. Compared with the substrate, whose potential variation as a function of time (s) is around − 0.1 V, in OC ZrO_2Y deposited at 90 °C exhibits two abrupt drops of potential at around 1000 and 3000 seconds on exposing the sample to a solution of NaCl. These could be related to the presence of the micropores and micro-cracks observed *via* SEM. For the samples deposited at 265 °C and ARP, abrupt drops in the potential are not observed, and they exhibit a broader passivation zone in the potentiodynamic polarization tests in Figure 5(c).

SEM analysis performed on thin films of ZrO_2Y-Ni shows a higher presence of imperfections such as micropores and microcracks in this coating compared to the ZrO_2Y films deposited under the same conditions at both temperatures (Figures 3(A) to (C)). Furthermore, even parts of the delaminated film (gray arrows) can also be seen, which shows a low substrate-coating adhesion. For the sample ZrO_2YNi deposited at 90 °C in Figure 5(b), there is an abrupt drop in the potential at 800s of exposure to corrosive electrolyte, and unlike ZrO_2Y, the one deposited at 265 °C exhibits a consecutive sequence of potential drops of 4000 to 10000 seconds, consistent with the presence of the micropores and microcracks seen *via* SEM, Figure 3(A-a). This is reflected in the higher current density and therefore lower corrosion resistance of the film deposited at 265 °C compared to the bare steel (Figure 5(d)). Like the ZrO_2Y coating, the ZrO_2YNi films have fewer imperfections when they are subjected to post-deposit ARP.

In general, it can be seen that the ceramic coating decreases the corrosion current density and increases the pitting nucleation potential, with a much wider passivation zone compared to the uncoated substrate. The efficiency of the ARP at 265 °C under inert atmosphere is reflected in the increase in the passivation zone and the pitting nucleation potential of this coating. These results can be confirmed from Table III, where corrosion current densities lower than those of the steel for

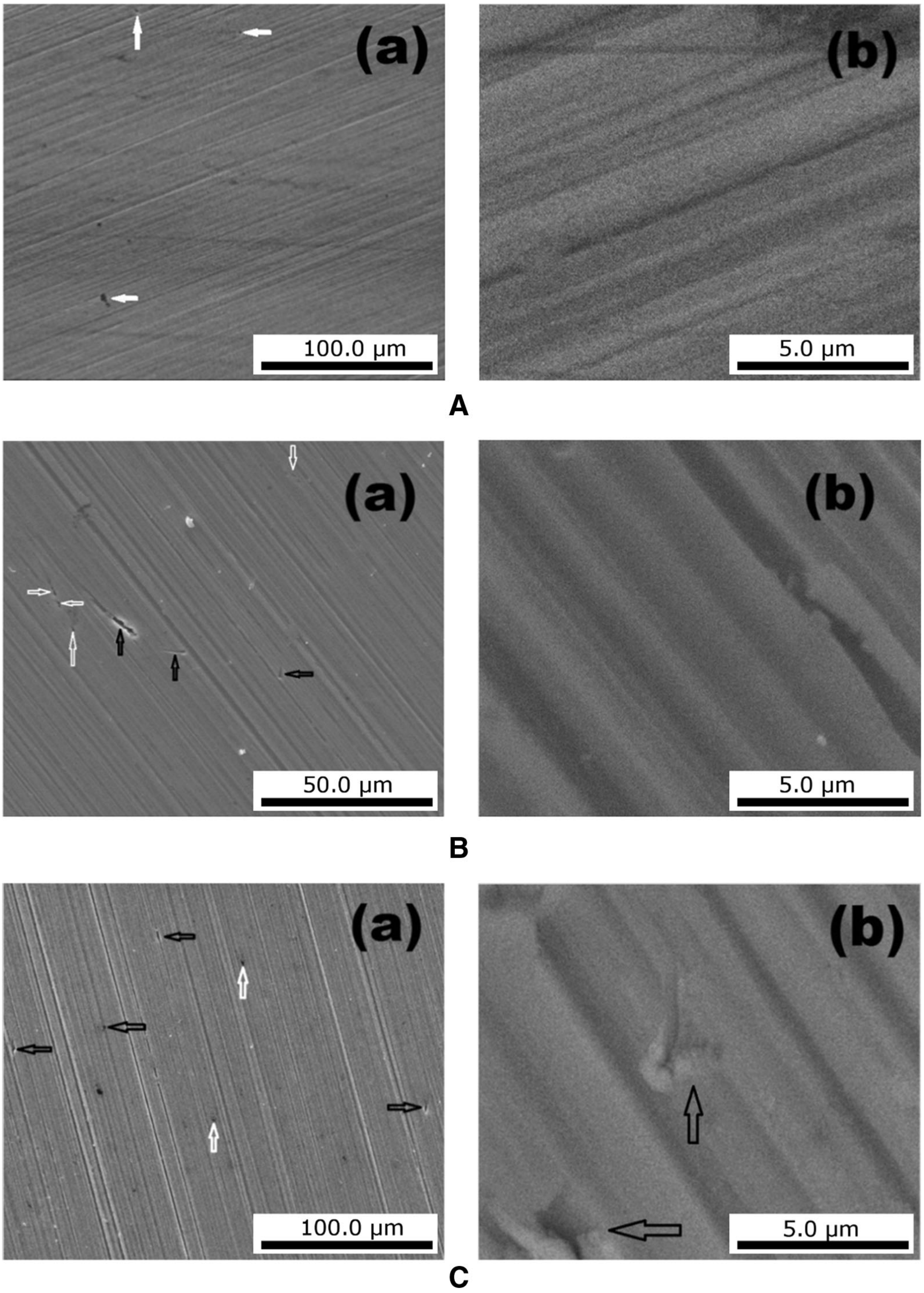

Fig. 2—SEM micrograph showing the morphology of the coatings ZrO_2Y-316L deposited at (*A*) 265 °C, (*B*) 90 °C, and (*C*) 90 °C ARP. (a) 1000 times, (b) 20,000 times.

the coated sample and an increase of one order of magnitude in the polarization resistance Rp can be seen. The ZrO_2Y films deposited at 90 °C without ARP exhibited the lowest corrosion resistance and, according to their surface morphology, exhibited the highest density of surface imperfections (Figure 2(B-a)). For the samples with added nickel, the current density is approximately of the same order as the samples without nickel, but the influence of surface imperfections of the samples with nickel is reflected in the fall of the nucleation potential of the pit at approximately 0.25, 0.60, and 0.70 V at 90 °C, 265 °C, and ARP, respectively.

The decrease in the corrosion current density of the films deposited from the ZrO_2Y/Ni target at 90 °C compared to the substrate indicates their higher

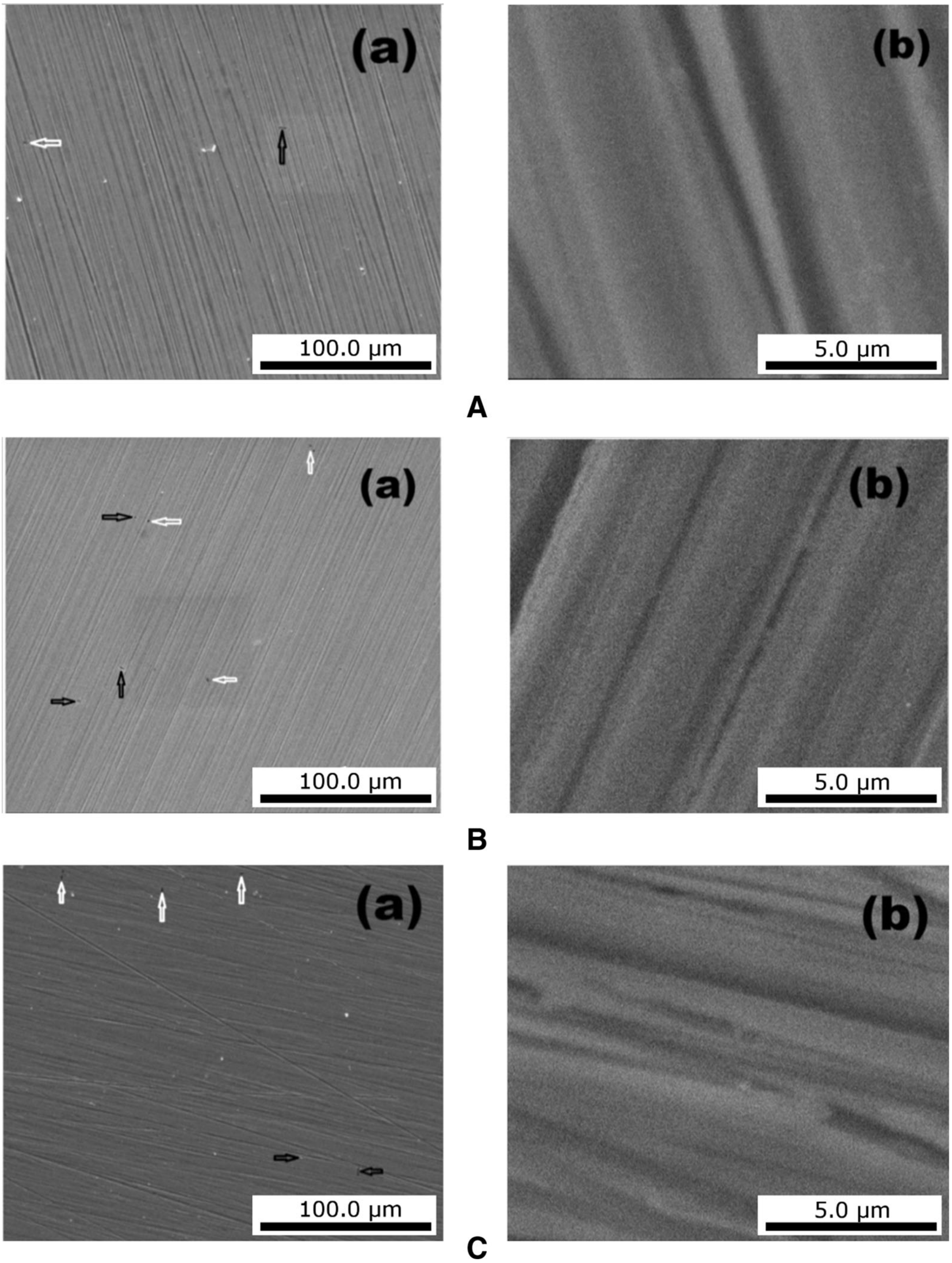

Fig. 3—SEM micrographs showing the morphology of the ZrO_2YNi-316L coatings deposited at (*A*) 265 °C, (*B*) 90 °C, (*C*) 90 °C after ARP. (a) 1000 times, (b) 20,000 times.

resistance to corrosion; however, when compared with those obtained under the same conditions from the ZrO_2Y target, it can be seen that in all cases the addition of nickel to the target increases the corrosion current density and decreases the pitting nucleation potential, except for the film deposited at 90 °C, where the pitting nucleation potential is approximately of the same order for the samples with and without nickel (Figure 5(d)).

It is well known that transition metal oxynitrides protect stainless steel by increasing their corrosion resistance.[14,15] ZrO_2YN15, $ZrO_2YNiN15$, and $ZrO_2YZnN15$ thin films were deposited *via* RF sputtering on AISI-316L in order to verify the efficiency of the ARP. Zinc was added with the aim of generating pores and imperfections in the oxynitride layer, due to the difference of atomic radio, 29 pct greater compared to Zr, and the difference in the crystalline structure and the

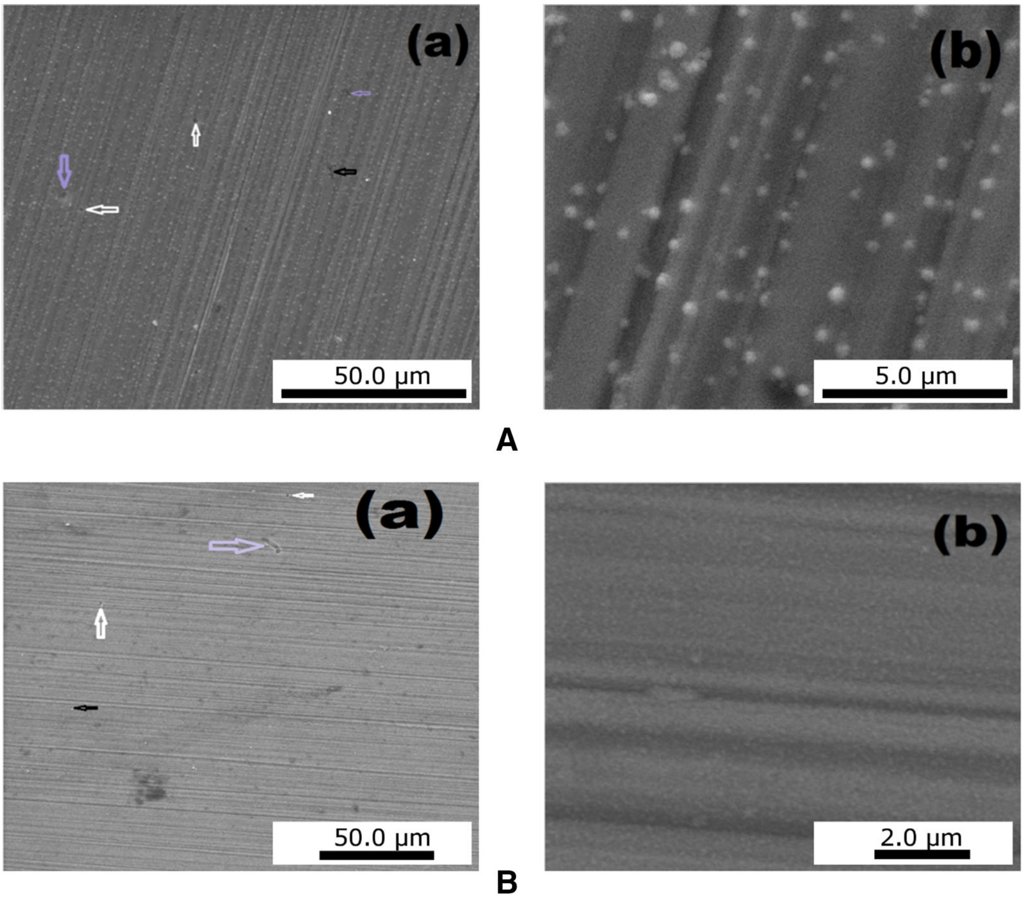

Fig. 4—SEM micrograph showing the morphology of the coatings ZrO_2YZn-316L deposited at (*A*) 265 °C and (*B*) 265 °C ARP. (a) 1000 times, (b) 20,000 times.

electronegativity. The $ZrO_2YZnN15$ film was only deposited at 265 °C and then was ARP at the same temperature, because when deposited at 90 °C, delamination of the coating occurred. In Figure 6, the OC and the potentiodynamic polarization curves for ZrO_2YN15-316L and $ZrO_2YNiN15$-316L can be observed; for these two types of coating, the nickel-free oxynitride is much more stable (Figures 6(a) and (b)). The ARP increases the corrosion resistance, as observed. The OC shows consecutive drops of potential associated with surface imperfections for the films deposited at 90 °C and 265 °C, while for the films with ARP, the OC stabilizes quickly during the three hours by the increase of an order of magnitude in the polarization resistance and decrease in corrosion current density in samples treated with ARP compared to untreated and steel samples (Table III and Figures 6(c), (d)).

For zirconium oxynitride with zinc, the OC confirms the results observed *via* SEM. The film without ARP exhibits more frequent drops of potential than the coatings of oxynitrides with and without nickel, associated with imperfections of the coating. As for ZrO_2Y, ZrO_2YN15, and $ZrO_2YNiN15$, the ARP treatment decreases the presence of imperfections, as can be seen by the stability of the potential for the OC and the corrosion current density lower by an order of magnitude for the ARP film, Figures 7(a) and (b).

1. *Morphology and composition post corrosion*

The study of the morphology and the composition of the films after the corrosion test in 3.5 pct NaCl solution generally revealed three different types of behavior: (I) delamination of the film and dissolution of the substrate in the corrosion zone, characteristic of the samples deposited at 265 °C, where there is total loss of the film; (II) delamination of the coating in the corrosion zone, characteristic of the films deposited at 90 °C, with the presence of zirconium in the corrosion zone; and (III) a zone of corrosion with very little deterioration of the coating and without change of composition, characteristic of zirconium oxynitride, (ZrO_2YN15). In Figure 8, one of the samples corresponding to the behavior type (I) is shown. Figure 8(a) shows the area where the corrosion test was performed, showing the substrate completely exposed. Figure 8(b) shows the limits of the corrosion zone where the diffusion of the electrolyte penetrates the film and detaches it from the substrate, and 8c shows in detail the area where once the coating has delaminated, the electrolyte initiates the process of dissolution of the substrate. The composition in the corrosion zone

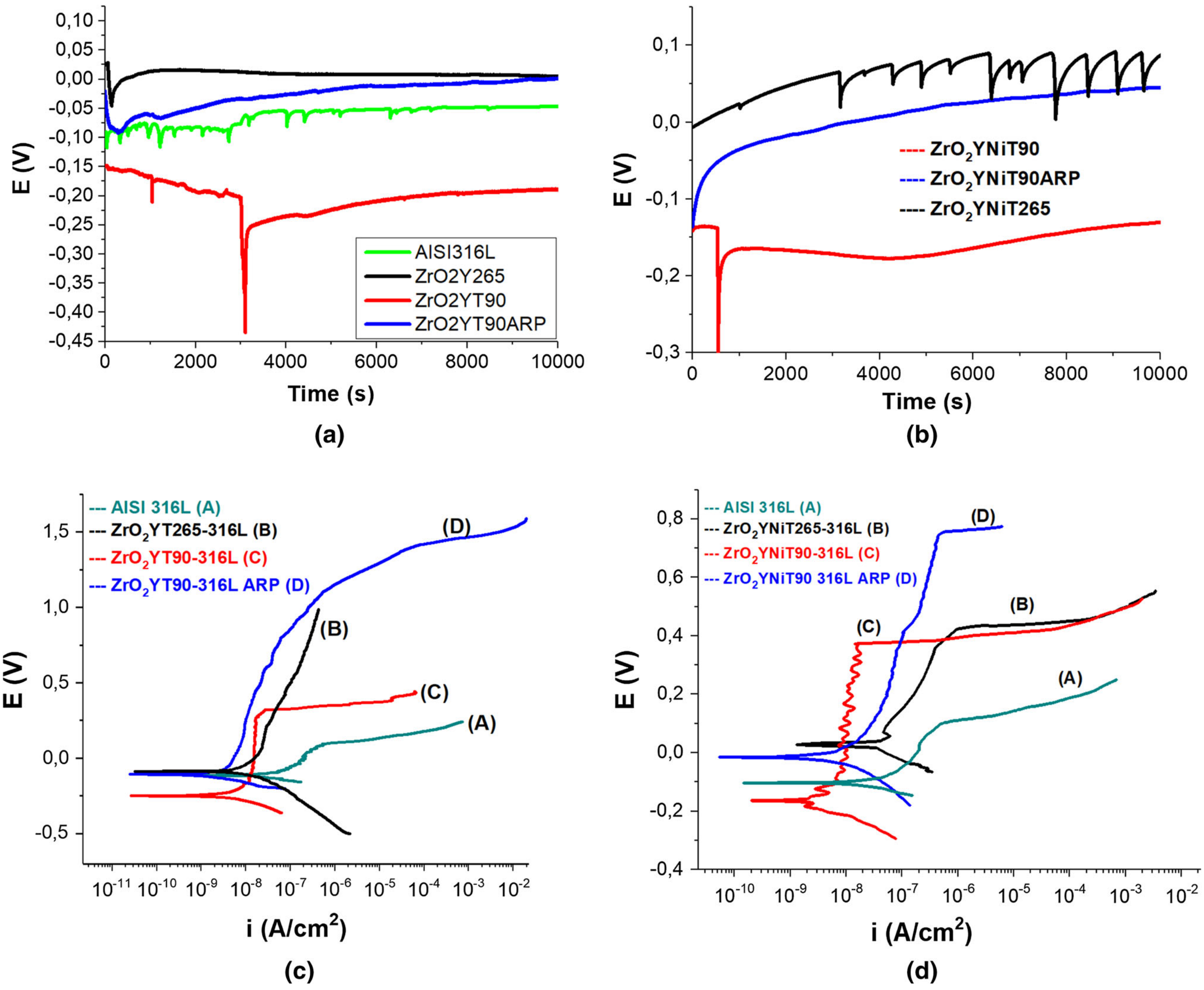

Fig. 5—Corrosion tests of samples in 3.5 pct NaCl solution (*a*) OC ZrO_2Y-316L, (*b*) OC ZrO_2YNi-316L, (*c*) potentiodynamic polarization ZrO_2Y-316, and (*d*) potentiodynamic polarization ZrO_2YNi-316L. Bare AISI-316L is introduced as a reference.

determined from EDX corresponds to 316L steel and at the edge to zirconia.

In Figure 9, in the SEM micrograph showing the attack area of the ZrO_2YT90-316L coatings deposited at 90 °C, delamination of the coating can be seen, but unlike the behavior type (I), there is no evidence of a strong attack on the substrate. The chemical composition in the corrosion zone shows the presence of the substrate alloy elements and ZrO_2Y of the coating.

The coatings of ZrO_2YNi and ZrO_2YZn exhibited behavior type (II), as shown in Figure 10(a), where in the unexposed area the chemical composition corresponds to that of the original coating, with Figure 10(b) showing low electrolyte diffusion towards the unexposed area. Finally, in the corrosion zone, there is evidence of the alloy elements of the steel and the coating, Figure 10(c).

Finally in Figure 11, the SEM micrograph shows the attack zone of the coatings ZrO_2YN15T90-316L ARP deposited at 90 °C, an area that has withstood the attack of corrosive electrolyte, where although there are signs of electrolyte leakage, the coating has not detached. The chemical composition is very close to that of the sample not exposed to corrosion.

As for the morphology *via* AFM, homogeneous films can be seen without an appreciable variation in their roughness, independent of the heat treatment, but with variation in the grain size. As an example, the results for the samples of ZrO_2YN15 with and without nickel are shown in Table IV. It can be seen that the films deposited at 265 °C and those ARP have a similar grain size, and 20–28 pct higher than those deposited at 90 °C without ARP. As for the effect of nickel, it can be seen that under the same deposition conditions, the roughness of films with nickel is lower. For ZrO_2YNiN15, the roughness is 39 pct less compared to ZrO_2YN15 deposited at 90 °C. If they are also matured, the difference in roughness is 22 pct.

C. *Chemical Composition*

Figure 12 shows the high-resolution XPS spectra for O 1*s*, N 1*s*, Zr 3*d*, and Y 3*d*. Their Gaussian-Lorentzian

Table III. Results of the Corrosion Test

Sample	I_{corr} (nA/cm^2)	E_{corr} (V)	Rp (GΩ cm^2)	Corrosion Rate (mmPY) $\times 10^{-4}$	PNP (V)
AISI 316L	55.6	− 0.114	0.47	4.32	0.103
ZrO_2Y T265-316L	12.3	− 0.087	2.11	9.57	—
ZrO_2Y T90-316L	6.10	− 0.250	4.24	4.76	0.319
ZrO_2Y T90-316L ARP	2.70	− 0.116	9.72	8.20	1.100
ZrO_2YNi T265-316L	74.2	0.018	0.35	5.76	0.426
ZrO_2YNiT90-316L	4.50	− 0.172	5.90	0.342	0.364
ZrO_2YNiT90-316L ARP	2.20	− 0.017	11.7	0.173	0.751
ZrO_2YN15T265-316L	30.4	− 0.024	0.86	2.37	0.194
ZrO_2YN15T90-316L	32.0	− 0.281	0.81	2.48	0.493
ZrO_2YN15T90-316L ARP	9.40	− 0.317	2.77	0.728	1.170
ZrO_2YNiN15T265-316L	30.4	− 0.024	0.86	2.37	0.194
ZrO_2YNiN15T90-316L	77.1	− 0.138	0.34	5.99	0.266
ZrO_2YNiN15T90-316L ARP	4.50	− 0.167	5.80	0.348	0.616
$ZnZrO_2$YN15T265-316L	33.9	− 0.204	7.67	2.63	0.170
$ZnZrO_2$YN15T265-316L ARP	2.70	− 0.174	9.60	0.210	0.249

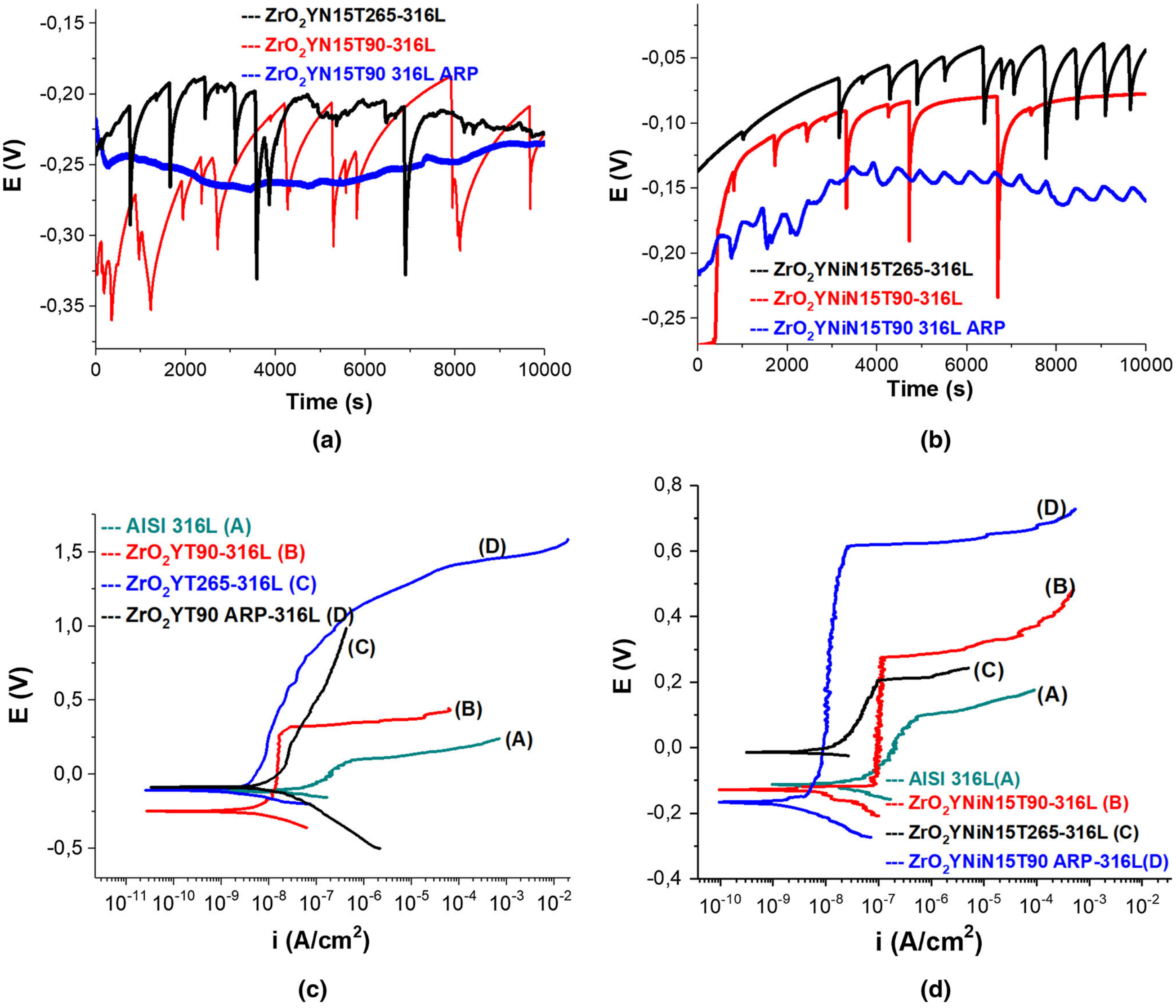

Fig. 6—Corrosion tests of samples in 3.5 pct NaCl solution (*a*) OC ZrO_2YN15-316L, (*b*) OC ZrO_2YNiN15-316L, (*c*) potentiodynamic polarization ZrO_2YN15-316, and (*d*) potentiodynamic polarization ZrO_2YNiN15-316L. Bare AISI-316L is introduced as a reference.

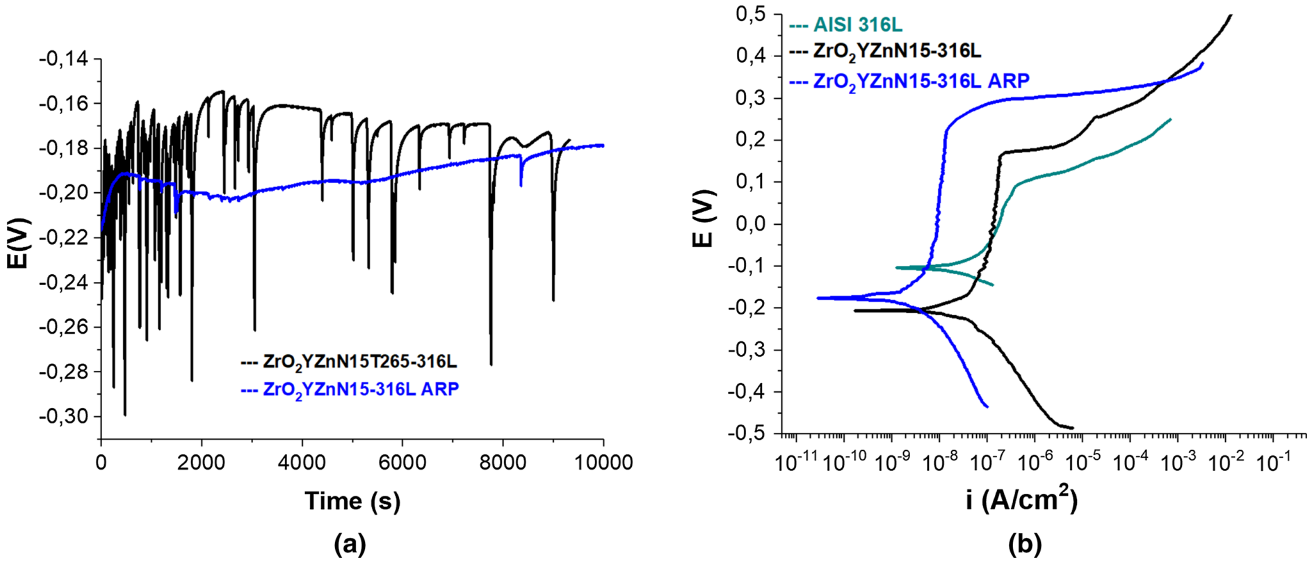

Fig. 7—Corrosion tests of samples tested in 3.5 pct NaCl solution (*a*) OC $ZrO_2YZnN15$-316L, (*b*) potentiodynamic polarization $ZrO_2YZnN15$-316L. Bare AISI-316L is introduced as a reference.

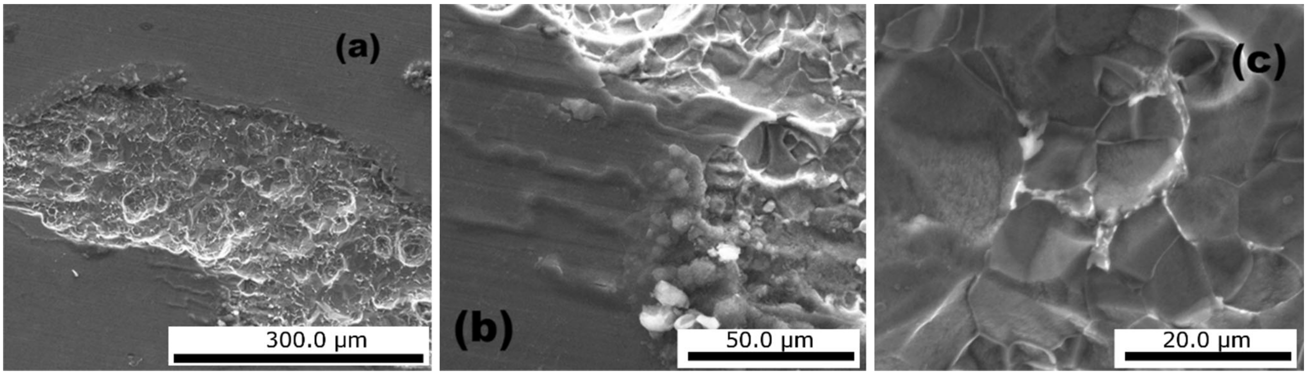

Fig. 8—SEM micrograph showing attack area of the coatings ZrO_2YT265-316L deposited at 265 °C. (*a*) Corrosion zone, (*b*) interface corrosion zone-coating, and (*c*) 5000 times magnification in corrosion zone.

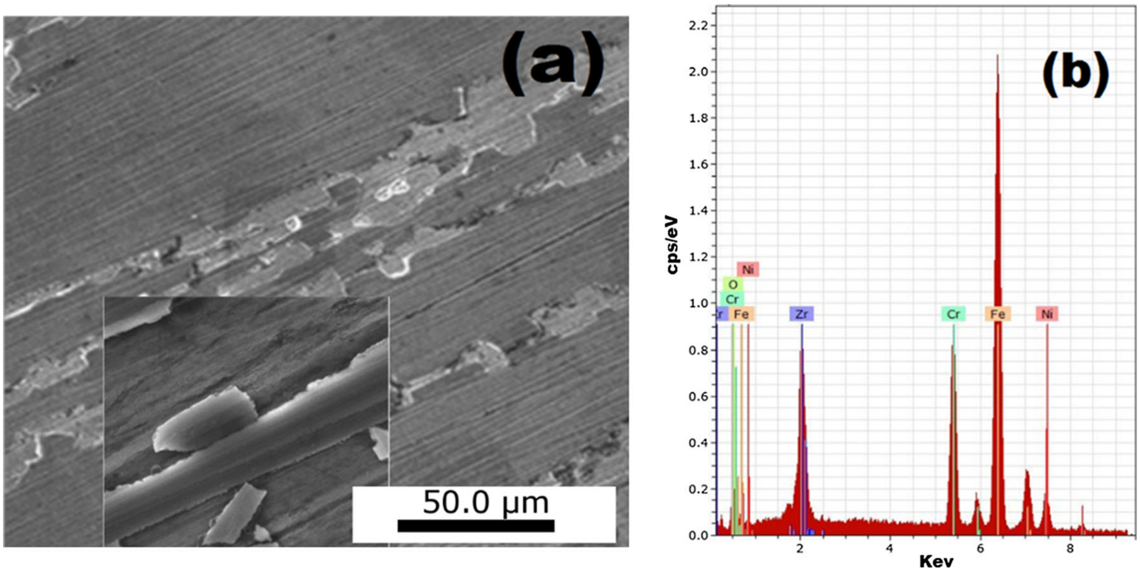

Fig. 9—SEM micrograph showing: (*a*) attack zone of the coatings ZrO_2YT90-316L deposited at 90 °C, (*b*) chemical composition coatings.

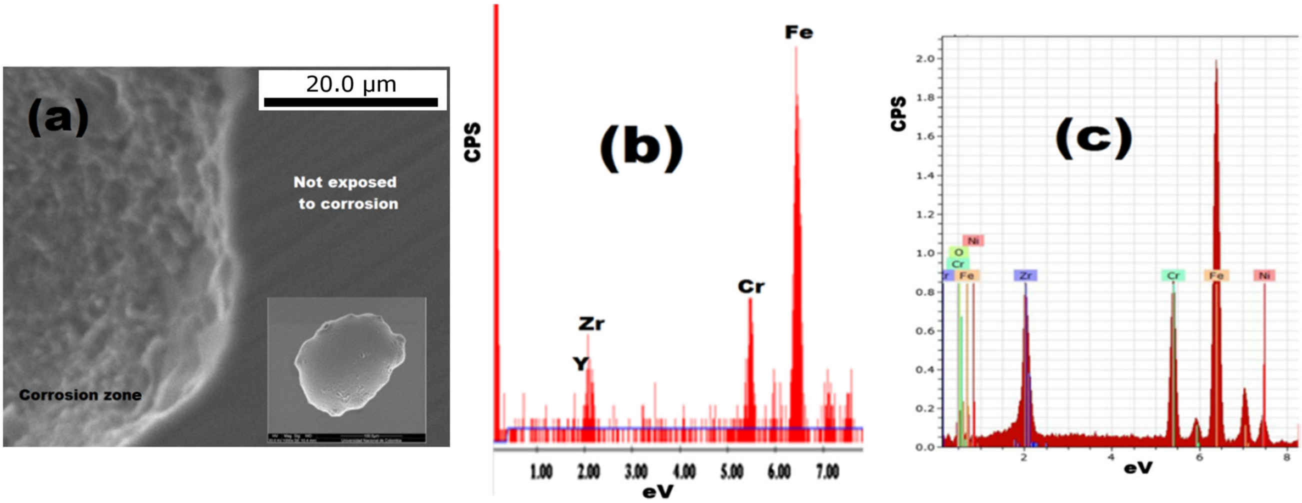

Fig. 10—SEM micrograph showing attack zone of the coatings ZrO_2ZnT265-316L deposited at 265 °C. (*a*) Corrosion zone-coating interface, (*b*) EDX in zone not exposed to corrosion, and (*c*) EDX in corrosion zone.

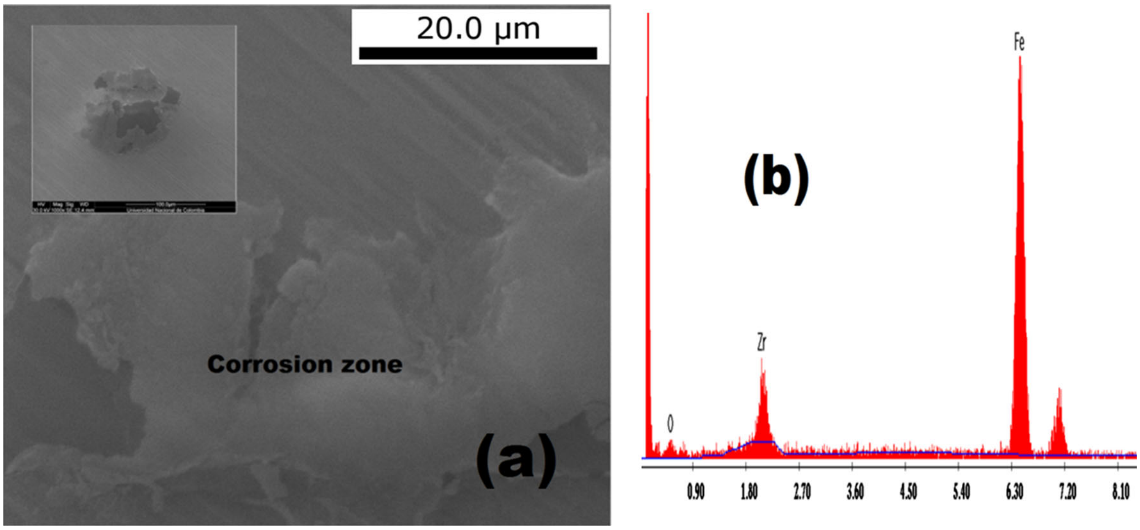

Fig. 11—SEM micrograph showing attack area of the coatings ZrO_2YN15T90-316L ARP deposited at 90 °C. (*a*) Corrosion zone and (*b*) chemical composition in corrosion zone.

resolved curve fit is shown. For the binding energy of O1*s* deposited at 90 °C and 265 °C, Figure 12(a), there is no representative difference in the chemical composition of the coating (Figure 6(b)). Two phases are present: ZrO_2, with a binding energy of 530.2 eV, which has been reported by several authors,[16–20] and ZrO_xN_y, with a binding energy of 531.7 eV.[17,19] The area under the curve of the spectra shows that the predominant oxide is ZrO_2, at 92 pct.

The N 1*s* core level spectrum for the film deposited at 265 °C (Figure 12(b)) can fit into one contribution centered at 395.8 eV, and in the case of film deposited at 90 °C, this contribution is centered at 396.2 eV. This energy has been associated by Signore and Rizo *et al.* with the Zr_3N_4 phase in thin films deposited *via* cathodic spray from a zirconium target.[16,18] However, in the present investigation, the films were deposited from a zirconia target partially stabilized with yttria. Due the high chemical stability of the zirconia and the low percentage of nitrogen substitution by oxygen reported by different authors in the formation of oxynitrides,[16–19] it would be chemically unlikely to completely substitute oxygen with nitrogen for nitride formation, so this binding energy could be associated with the zirconium oxynitride species. Milosev *et al.* report the same binding energy for the formation of titanium oxynitride.[20] On the other hand, according to the area under the signal curve N 1*s* (Figure 12(b)), a higher nitrogen composition can be seen for the film deposited at 90 °C, *i.e.*, at this temperature, it increases the incorporation of nitrogen in the crystalline structure of zirconia. The increase in kinetic energy of the nitrogen atoms associated with the higher temperature would prevent the accommodation of nitrogen atoms in the vacant spaces of the crystalline structure of zirconia at 265 °C.

Table IV. Roughness and Grain Size of ZrO_2YN15 and ZrO_2YNiN15 Coatings

	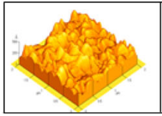	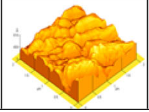	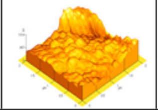	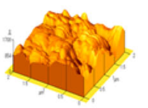	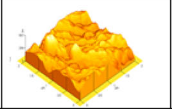	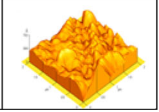
Sample	ZrO_2YN15T90	ZrO_2YN15T90 ARP	ZrO_2YN15T265	ZrO_2YNiN15T90	ZrO_2YNiN15T90 ARP	ZrO_2YNiN15T265
Size grain (µm)	0.26±0.07	0.36±0.07	0.30±0.01	0.27±0.08	0.33±0.08	0.28±0.08
Roughness RMS (nm)	12.40±0.02	13.60±0.04	8.06±0.02	7.54±0.01	3.05±0.01	7.96±0.02

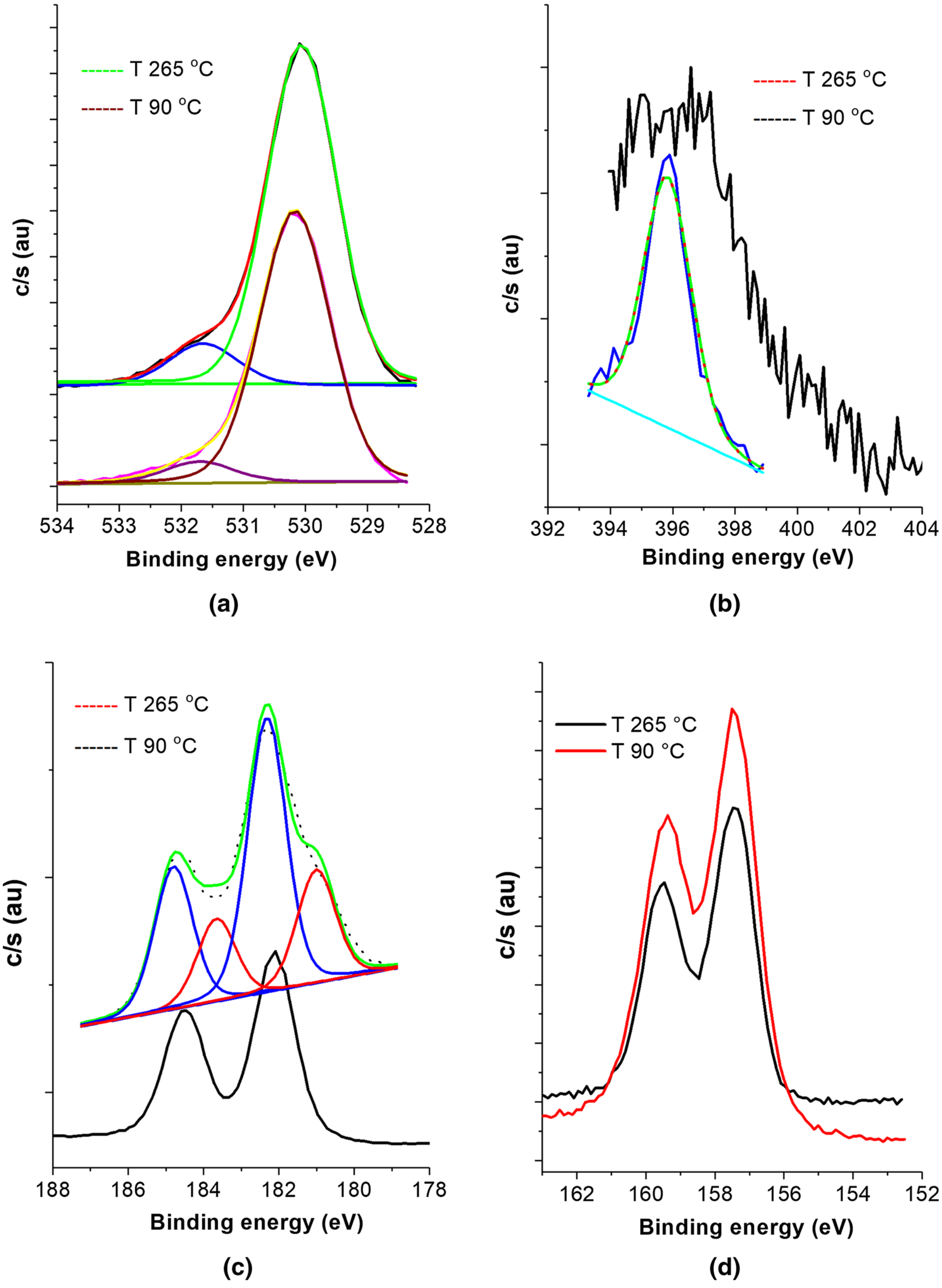

Fig. 12—High-resolution XPS spectra of ZrO_2YN15, for (*a*) O 1*s*, (*b*) N 1*s*, (*c*) Zr *3d*, (*d*) Y *3d* deposited at 90 °C and 265 °C and after cleaning with Ar^+ for 1 min.

In Figure 12(c), the binding energies associated with the Zr 3*d* deposited at 265 °C exhibit two doublets: $3d_{5/2}$ at 181.01 eV and $3d_{3/2}$ at 183.66 eV, assigned to ZrO_xN_y, with a separation of 2.7 eV, and $3d_{5/2}$ at 182.32 eV and $3d_{3/2}$ at 184.8 eV, assigned to ZrO_2, separated by 2.5 eV. A similar profile for the Zr 3*d* signal has been reported by Wong and Cheong[21] in the formation of ZrO_xN_y by simultaneous oxidation and nitridation in the nitrous oxide of sputtering Zr on SiC substrate, and in a previous article we found zirconium oxynitride deposited *via* RF sputtering from a zirconium target.[22] This separation in the spin doublet of 2.5 eV is closer to that of the zirconium (2.4 eV),[23] and it is associated with the electronegativity decrease provoked by the partial substitution of O by N in ZrO_2, in such a way that N diffuses across the surface and two phases are simultaneously formed (ZrO_2 and ZrO_xN_y). In Figure 6(d), it can be seen from the composition spectrum for Y 3*d* that there are no representative changes in the binding energy of the yttrium oxide for the two deposition temperatures.

IV. CONCLUSIONS

Porous ZrO_2Y, ZrO_2YNi, ZrO_2YN15, $ZrO_2YNiN15$, and $ZrO_2YZnN15$ thin films partially stabilized with 8 pct mol Y_2O_3 were deposited on AISI-316L. The surface morphology, determined *via* SEM, showed that the films were porous and exhibited the presence of imperfections. To reduce their porosity and increase corrosion resistance, ARP was carried out for two hours in an inert Ar atmosphere under reduced pressure. The films thus obtained were characterized by an increase in the corrosion resistance of AISI-316L and the passivation zone between 0.3 and 1.2 V.

ACKNOWLEDGMENTS

This research was supported by the Fundación para la Promoción de la Investigación y la Tecnología, Asociación de Universidades Iberoamericanas, Ministry of Economy, Industry and Competitiveness of Spain/FEDER Program of the EU (MAT 2013-40823-R, MAT2014-60857-R, and CTQ2015-68951-C3-3-R), CSD2009-00013, and Universidad Nacional de Colombia Proyect DIB 35637.

REFERENCES

1. X. Chen, Q. Fu, Y. Jin, M. Li, R. Yang, X. Cui, and M. Gong: *Mater. Sci. Eng., C*, 2017, vol. 70, pp. 1071–75.
2. A. Qingbo, T. Huiping, W. Jianzhong, Z. Hao, M. Jun, and L. Bin: *Rare Metal Mater. Eng*., 2014, vol. 43 (10), pp. 2344–48.
3. N.F. Daudt, M. Brama, A.P. Cysne-Barbosa, and C. Alves: *Mater. Lett*., 2015, vol. 141, pp. 194–97.
4. M.A.H. Gepreela and M. Niinomi: *J. Mech. Behav. Biomed. Mater*., 2013, vol. 20, pp. 407–15.
5. L. Wanga, X. Hua, X. Maa, Z. Ma, Y. Zhang, Y. Lua, X. Li, W. Lei, and Y. Feng: *Colloids Surf. B*, 2016, vol. 148, pp. 440–52.
6. S. Jain, N.D. Budiansky, J.L. Hudson, and J.R. Scully: *Corros. Sci*., 2010, vol. 52, pp. 873–85.
7. N.H. Turner: D.E., Ramaker and F.L. Hutson*J. Electron. Spectrosc. Relat. Phenom*., 1993, vol. 63, pp. 117–30.
8. G.I. Cubillos, J.J. Olaya, D. Clavijo, J.E. Alfonso, and C. Cardozo: *Thin Solid Films*, 2013, vol. 529, pp. 342–46.
9. M. Stern and A.L. Geary: *J. Electrochem. Soc*., 1957, vol. 104, pp. 56–63.
10. A.W. Burton, K. Ong, T. Rea, and I.Y. Chan: *Microporous Mesoporous Mater*., 2009, vol. 117 (1–2), pp. 75–90.
11. R. Konar, J. Mukhopadhyay, A.D. Sharma, and R.N. Basu: *Int. J. Hydrogen Energy*, 2016, vol. 41, pp. 1151–60.
12. J. Joos, M. Ender, I. Rotscholl, N.H. Menzler, and E. Ivers-Tiffée: *J. Power Sources*, 2014, vol. 246, pp. 819–30.
13. J.J. Roa, M.A. Laguna-Bercero, A. Larrea, V.M. Orera, and M. Segarra: *Ceram. Int*., 2011, vol. 37, pp. 3123–31.
14. Z. Ba, Q. Dong, X. Zhanga, J. Wang, C. Yuan, and Y. Liao: *Surf. Coat. Technol*., 2016, vol. 294, pp. 67–74.
15. G.I. Cubillos, M. Bethencourt, and J.J. Olaya: *Appl. Surf. Sci*., 2015, vol. 327, pp. 288–95.
16. M.A. Signore, A. Rizzo, L. Mirenghi, M.A. Tagliente, and A. Cappello: *Thin Solid Films*, 2007, vol. 515, pp. 6798–804.
17. A. Rizzo, M.A. Signore, L. Mirenghia, and T. Di Luccio: *Thin Solid Films*, 2009, vol. 517 (21), pp. 5956–64.
18. A. Rizzo, M.A. Signore, L. Mirenghi, L. Tapfer, E. Piscopiello, E. Salernitano, and R. Giorgi: *Thin Solid Films*, 2012, vol. 520, pp. 3532–38.
19. D. Roman, J. Bernardi, C. de Amorim, F. de Souza, A. Spinelli, C. Giacomellid, C. Figueroa, I. Baumvol, and R. Basso: *Mater. Chem. Phys*., 2011, vol. 130, pp. 147–53.
20. I. Milosev, H.H. Strehblow, and B. Navingek: *Surf. Coat. Technol*., 1995, vols. 74–75, pp. 897–902.
21. Y.H. Wong and K.Y. Cheong: *Thin Solid Films*, 2012, vol. 520, pp. 6822–29.
22. G.I. Cubillos, M.E. Mendoza, J.E. Alfonso, G. Blanco, and M. Bethencourt: *Mater. Charac*., 2017, vol. 131, pp. 450–58.
23. J.F. Moulder, W.F. Stickle, P.E. Sobol, and K.D. Bomben: *Handbook of X-Ray Photoelectron Spectroscopy*, Perkin Elmer Corporation, Minnesota, MN, 1992.